

Sliding wear resistance of metal matrix composite layers prepared by high power laser

V. Ocelík, D. Matthews, J.Th.M. De Hosson*

Department of Applied Physics, Materials Science Centre and The Netherlands Institute for Metals Research, University of Groningen, Nijenborgh 4, 9747 AG Groningen, The Netherlands

Received 2 April 2004; accepted in revised form 10 September 2004
Available online 28 October 2004

Abstract

Two laser surface engineering techniques, Laser Cladding and Laser Melt Injection (LMI), were used to prepare three different metal matrix composite layers with a thickness of about 1 mm and approximately 25–30% volume fraction of ceramic particles.

SiC/Al–8Si, WC/Ti–6Al–4V and TiB₂/Ti–6Al–4V layers were prepared by a Laser Melt Injection process, whereby additional material in the form of ceramic particles is injected into the molten substrate. As a result, a microstructure characterized by hard ceramic particles distributed in a metal matrix with very strong bonding is formed in the surface layer of the treated metal.

A TiB₂/Ti–6Al–4V metal matrix composite layer was produced on Ti–6Al–4V substrates by conventional laser cladding. A mixture of TiB₂/Ti powders has been used as a precursor to obtain two microstructurally distinct layers, namely eutectic and primary TiB particles dispersed in the Ti–6Al–4V matrix.

Sliding wear properties of these metal matrix composites layers were studied at boundary lubrication conditions and compared with the wear of the substrate materials. The observed wear mechanisms are summarized and related to detailed microstructural observations. The layers have been found to show excellent interfacial bonding, coupled with dramatically improved tribological properties expressed through a relative wear resistance value ranging from 30 to 1500.

© 2004 Elsevier B.V. All rights reserved.

Keywords: Laser surface treatment; Wear; Scanning Electron Microscopy; Microstructure; Carbides; Borides; Metal matrix composites

1. Introduction

It is well documented that light metals such as aluminum, titanium and their alloys are characterized by low density (relative to other structural metals and alloys), excellent corrosion resistance and (specifically titanium) high specific mechanical strength. However, the range of applicability is limited by their poor tribological functionality, which for pure titanium is related to its low *c/a* ratio as a HCP metal [1]. As such, many attempts have been made to process light metal alloys through a diverse range of surface engineering technologies.

Laser cladding is one such surface engineering technique, an extension of which is Laser Melt Injection (LMI). In a LMI technique, a high power laser locally melts the top part of a metal substrate whilst, simultaneously, a powder is injected into the melt pool [2]. The process slightly differs to laser cladding, which incorporates the additional material into the substrate in a molten state, since during LMI there is an aim of limited interaction between ceramic particles and laser beam, and therefore the particles are injected still in a solid state. A laser track, reinforced with particles [3], is consequently formed.

These methods are accordingly suited to the formation of thin MMC layers on the top of a metal work-piece for improving the mechanical and tribological properties. MMCs have been realized as bulk materials for some time, and afford many advantages in industrial applications. The

* Corresponding author. Tel.: +31 503634898; fax: +31 503634881.

E-mail address: hossonj@phys.rug.nl (J.Th.M. De Hosson).

properties of the produced MMC layer depend on, among other things, the amount of the injected powder, the microstructure of the melt pool matrix and the bonding between particle and matrix. Since the wetting properties between ceramic and metal materials are usually poor [4,5], the bonding between particle and matrix may cause a severe problem. To circumvent this problem, the combination of a substrate with ceramic particles that present a high affinity for each other was chosen. The consequence is that reaction layers between the particles and matrix may be formed [6,7], which may improve the wetting and may therefore improve the bonding [5].

In this paper, Al–8Si and Ti–6Al–4V alloys represent the substrate materials, proven to be suitable for laser processing [8–12] and investigation surrounds the formation of SiC/Al–8Si, WC/Ti–6Al–4V (both single and multigrain WC particles were used) and TiB_x /Ti–6Al–4V MMCs. TiB_2 particles were also clad on a Ti alloy matrix and TiB needles were formed by an exothermically induced reaction from a TiB_2 /Ti mixture of particles during cladding. Previous research [8,9,13,14] produced microstructural information with respect to processing parameters, microstructure evolution, microstructural orientation relationships and properties. It is intended that this work will complete the previous works with some further microstructural observations and extend the investigation into wear and friction characteristics of the clad layers.

2. Experimental

Commercially available Al–8Si cast alloy and Ti–6Al–4V alloy were used as substrates for preparing single tracks of SiC/Al–8Si, WC/Ti–6Al–4V and TiB_2 /Ti–6Al–4V MMC layers by the LMI technique using a 2 kW Rofin Sinar Nd:YAG laser. SiC particles with a mean size of 60 μm , globular multigrain WC particles with a mean size of 80 μm , single grain WC particles with a size of 10–30 μm and a mixture of TiB_2 (5–25 μm) and Ti particles (90 μm) particles were injected under LMI processing conditions. A more detailed description of the LMI process, with particular reference to the process parameters as well as a detailed description of microstructures and particle distributions formed inside SiC/Al–Si, WC/Ti–6Al–4V and TiB_2 /Ti–6Al–4V layers can be found elsewhere [8,9].

Laser-clad layers, which produced eutectic and primary TiB microstructures, were fabricated employing the same precursor as for TiB_2 /Ti–6Al–4V LMI MMCs, and various processing parameters used can be found elsewhere [14].

Optical microscopy (Olympus Vanox-AHMT) and Scanning Electron Microscopy (SEM Philips XL30 FEG with energy dispersive X-ray spectroscopy (EDS)) were used to study the MMC layers. In addition, Orientation Imaging Microscopy (OIM attachment to Philips XL30s FEG) and X-ray diffraction (XRD Philips PW-1830) were used to study particle distribution, microstructure and microstruc-

tural relationships in MMC layers prepared by LMI and laser cladding.

Samples for the wear tests were cut from 10 mm thick substrates (5 mm in case of Ti–6Al–4V substrate) by spark erosion with dimensions of $10 \times 10 \times 1$ and $10 \times 5 \times 1$ mm³, respectively. Tests were performed using a Plint Tribometer TE 67 using pin-on-disk setup. A stationary specimen is pressed under known normal force against the surface of rotating disk of 100Cr6 hardened (60 HRC) steel with an initial surface roughness of $R_a=0.1$ μm . The specimen and ring were completely submerged in an oil bath (BP Transcal N) at room temperature. The friction force and the change of relative position between pin and ring were measured continuously during 20 h of wear testing, and the friction coefficient was directly calculated. To exclude hydrodynamic lift effects and to perform wear tests under boundary lubrication conditions, wear experiments were performed at a low constant sliding speed (0.01 m/s) and with contact pressures of 20 and 100 MPa. SEM in Secondary Electrons (SE) mode or Back-Scattered Electrons (BSE) mode, EDS and confocal optical microscopy (μ Surf Nanofocus Messtechnik) were employed to inspect the worn surfaces after the tests.

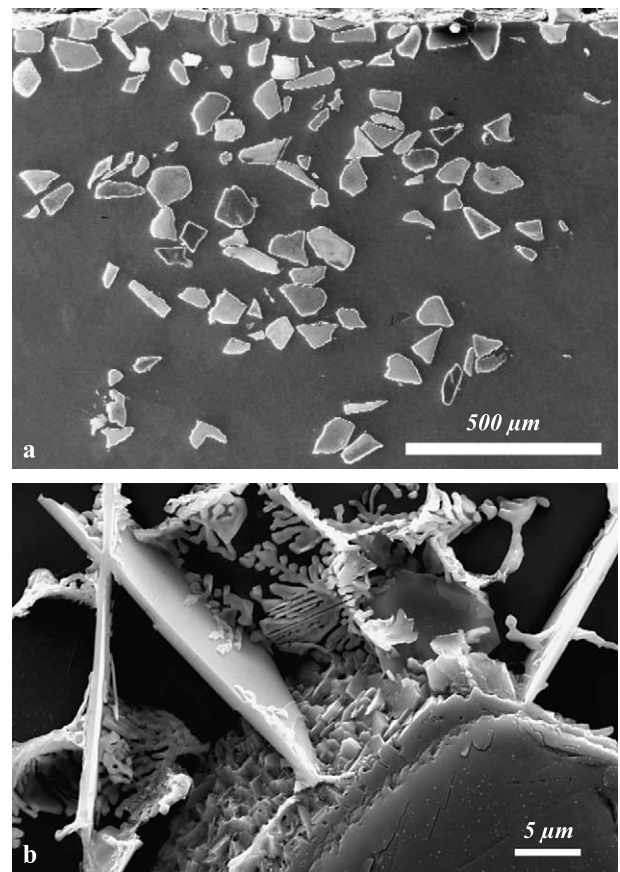


Fig. 1. SEM micrographs of SiC/Al–8Si MMC prepared by laser melt injection. (a) Perpendicular cross-section of a single laser track; (b) the same sample deep etched: Al matrix removed around a corner of an injected SiC particle. Large Al_4C_3 plates and Si netting from Al–Si eutectic are present. Small Al_4C_3 plates at the SiC/Al interface are visible.

3. Results

3.1. Microstructure of MMC layers

It has previously been identified that the processing window for LMI in pure Al is relatively small [8], due to the presence of a strong oxide skin layer on the top of the melt pool and due to the small size of the melt pool behind a scanning laser beam caused by the high thermal conductivity of Al. Fig. 1 demonstrates the distribution of SiC injected into the Al–8Si alloy substrate and the local microstructure formed in a surrounding of each SiC particle. Aluminum grains with grain size of about 50–100 μm form the matrix. The grains contain large amounts of dendrites with a length of about 5 μm . Al–Si eutectic fills the interdendritic space. SiC particles were partially dissolved during the injection process and large Al_4C_3 plates are observed in the matrix of the melt pool. A large amount of small parallel Al_4C_3 plates is formed at the Al/SiC interface. It was proved by transmission electron microscope observation and by electron back-scattering diffraction that a strong orientation relationship between SiC particle and small Al_4C_3 plates exists [3].

The Ti–6Al–4V alloy represents a more convenient substrate to apply the LMI technique. Fig. 2a shows the

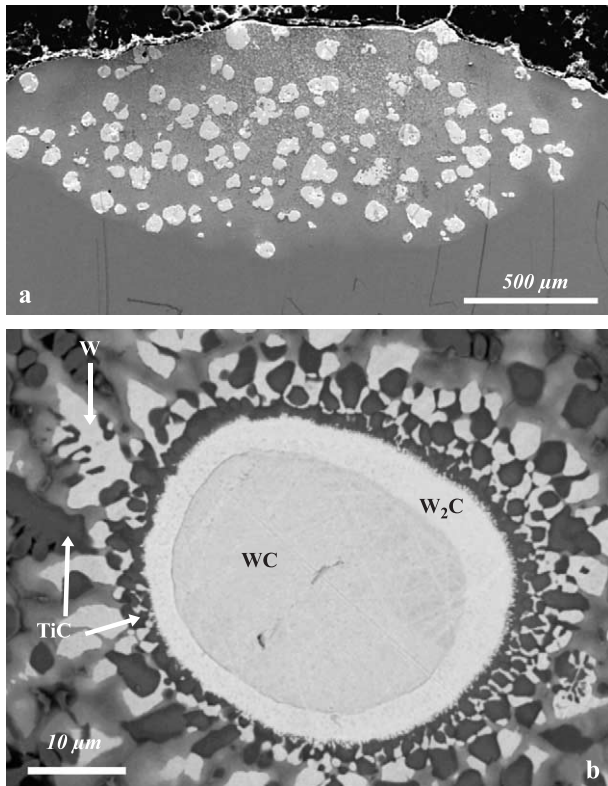


Fig. 2. SEM micrographs (BSE mode) of WC/Ti–6Al–4V MMC prepared by laser melt injection of multigrained WC particles. (a) Perpendicular cross-section of single laser track; (b) WC particle and reaction zone. The center of the WC particle is surrounded by a W_2C layer, which is further surrounded by a TiC layer. Next to this TiC layer pure W grains are present, alternated by individual TiC grains [9].

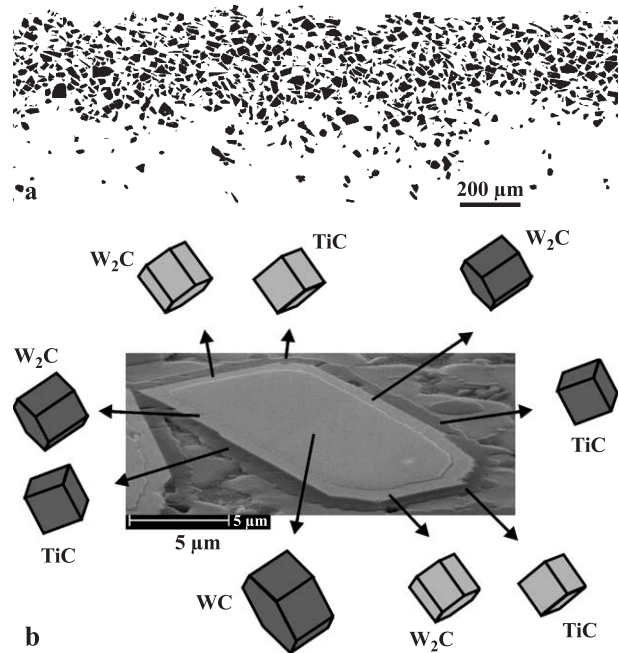


Fig. 3. SEM of the laser track of WC/Ti–6Al–4V MMC prepared by LMI of single grained WC particles. (a) SEM micrograph of longitudinal cross-section (BSE mode after ‘inversion’ and ‘threshold’ image manipulation) [16]; (b) SEM micrograph (70° oblique view) of the microstructure formed around individual WC particle. Orientation relationships detected by OIM are depicted.

cross-section of one laser track with injected WC particles consisting of many fused grains. As Fig. 2b (taken from Ref. [9]) demonstrates, the reaction zone between particle and metal matrix consists of different reaction layers. A W_2C layer surrounds the center of WC particle and next to the W_2C a TiC reaction layer is present, which is itself surrounded by W and TiC grains. Further TiC dendrites are present in the Ti–6Al–4V matrix. As it has been found that an intergranular fracture inside the center of WC particles limits the mechanical performance of this MMC [15], the functionally graded WC/Ti–6Al–4V MMC coating was prepared by injection of single grain WC particles [16]. Fig. 3a (taken from Ref. [16]) shows the distribution of injected WC particles on the longitudinal laser track cross-section and Fig. 3b demonstrates a microstructure around an individual WC particle together with the orientation relationships formed between the particle itself and its surrounding reaction layer. The microstructural analysis reveals the formation of new phases, similarly as during the injection of fused multi-grained WC particles into the same substrate. The W_2C (Trig. $P\bar{3}m2$) layer surrounds each WC (Hex. $P\bar{6}m2$) particle and is followed by the TiC (Cub. $Fm\bar{3}m$) layer. Individual TiC dendrites surrounded by Ti-alloy matrix are observed in the vicinity of injected WC particles. The thickness of the W_2C and TiC reaction layers depend on the injection depth. Near the layer surface they are both about 0.1–0.2 μm thick and their thickness increases almost linearly with the injection depth to reach the maximum values at the bottom of laser track; 1 μm for

W_2C and $1.8 \mu\text{m}$ for TiC layer, respectively. Crystallographic orientation relationships detected by OIM are also depicted in Fig. 3b. Quite often the orientation relationship in which the close-packed planes and directions are parallel between W_2C and TiC crystals is observed:

$$(0001)_{W_2C} \parallel (111)_{TiC}; [\bar{1}\bar{2}10]_{W_2C} \parallel [1\bar{1}0]_{TiC}. \quad (1)$$

The single crystal WC particles have their facets oriented in accordance with their crystallographic planes and therefore another orientation relationship is observed quite often, between the WC particles and W_2C layer:

$$(0001)_{W_2C} \parallel (0001)_{WC}; [\bar{1}\bar{2}10]_{W_2C} \parallel [\bar{1}\bar{2}10]_{WC} \quad (2)$$

As Fig. 3b demonstrates, both orientation relationships are fulfilled on the left and right side of WC particle, but only orientation relationship (Eq. (1)) is observed on its upper and lower side.

Finally, Fig. 4 (taken from Ref. [14]) shows three different microstructures, which may be achieved through the variation of cladding conditions, when a mixture of TiB_2 and Ti particles is clad on a Ti-6Al-4V substrate [14]. When the interaction between clad powder and laser beam is minimized, the laser melt injection regime prevails and a microstructure characterized by Fig. 4a prevails. Original TiB_2 particles are randomly distributed in a Ti-6Al-4V matrix and a reaction zone is formed around each particle consisting of TiB. Some TiB plates are also randomly distributed in matrix. Fig. 4b characterizes a microstructure, whereby mainly primary TiB plates are formed through the solidification from melted TiB_2 and finally the microstructure, which consists only of the fine eutectic TiB particles, is presented in Fig. 4c. These two different microstructures were achieved by variations in the main laser cladding conditions; laser power, which mainly controls the temperature, and scanning speed that determines the cooling rate [14].

3.2. Wear-friction results

Sliding wear tests were performed on single laser track MMC layers produced using optimum laser processing conditions presenting microstructures as shown in Figs. 1–4. The wear behavior of these surfaces was compared with that of the untreated substrate and with that of the substrate surface treated by a simple laser remelting, without injection of the ceramic particles. The common characteristic of the wear behavior, of all the samples, is that after some incubation and subsequent transition period, a constant wear rate is established, as can be seen in Figs. 5 and 6.

Fig. 5 shows the sliding distance dependencies of friction coefficient and wear, not only for the SiC/Al-8Si and WC/Ti-6Al-4V layers but also for the untreated surfaces and the remelted surfaces (the same laser processing parameters as during the laser melt injection were used). Some data curves

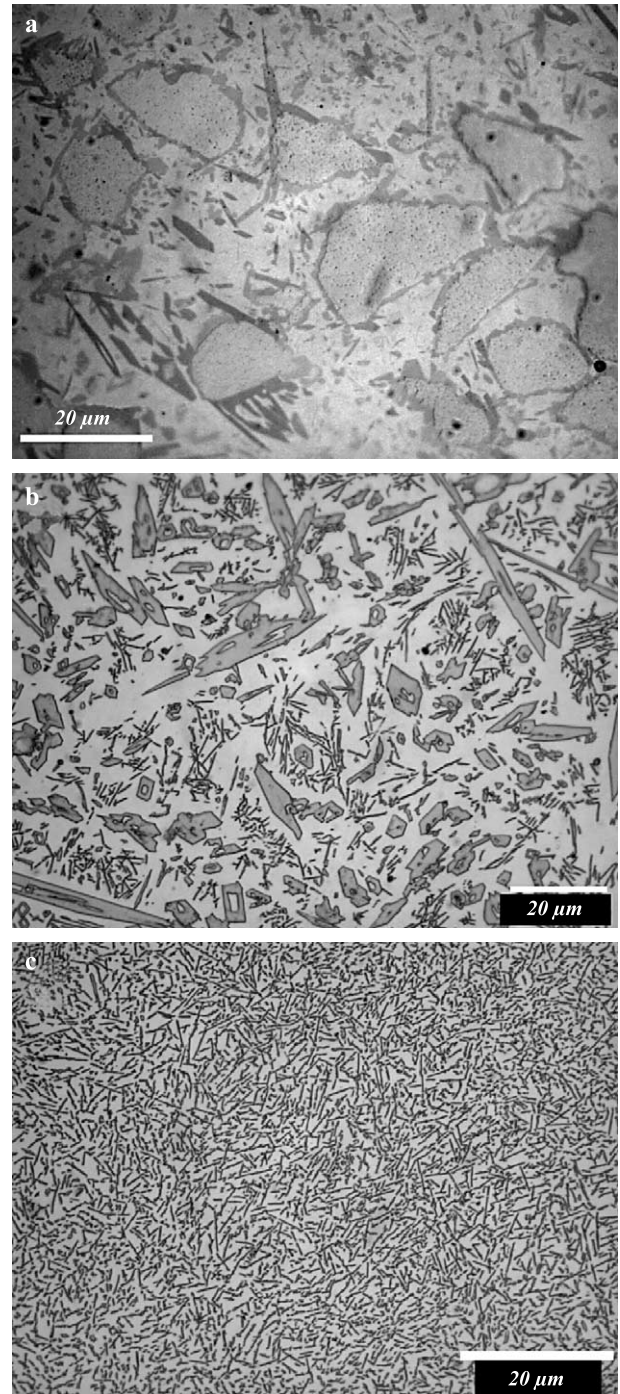


Fig. 4. Optical micrographs of different MMC microstructures simply achieved by a variation of laser processing conditions during the cladding of mixture of TiB_2 and Ti powders on Ti-6Al-4V substrate [14]: (a) original TiB_2 particles with TiB plate reaction around them and also distributed in the substrate matrix; (b) mainly primary TiB plates solidified from the melt; (c) eutectic TiB particles homogeneously distributed in the substrate matrix.

in Figs. 5 and 6 have been smoothed using a Savitzky-Golay linear smoothing procedure [17] to improve the clarity and some are plotted as recorded to demonstrate experimental data spread.

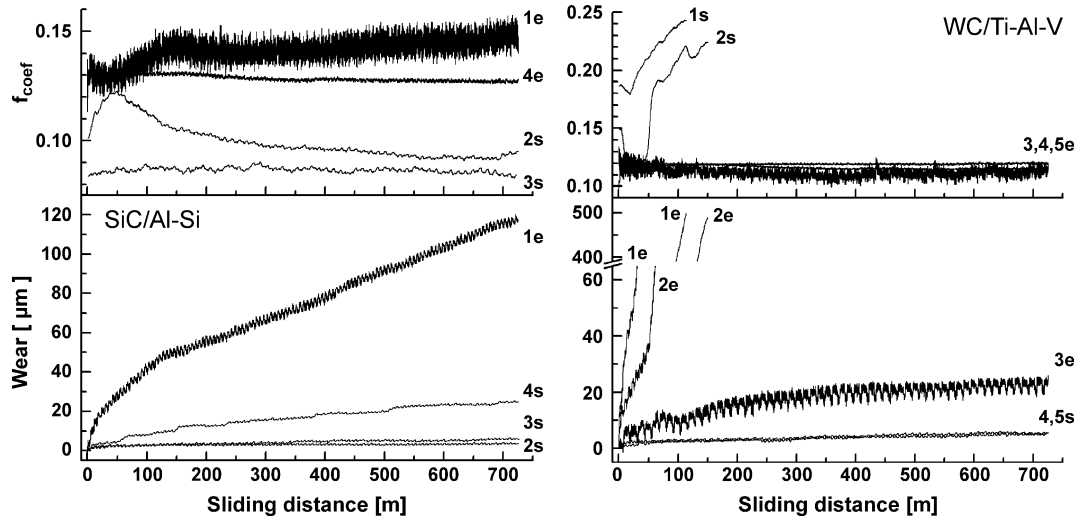


Fig. 5. Friction coefficient and wear versus sliding distance for SiC/Al-Si and WC/Ti-6Al-4V MMC coatings in comparison with non-treated surfaces. Curve 1—basic alloy; curve 2—basic alloy remelted by laser beam; curve 3—MMC layer tested at 20 MPa contact stress; curve 4—MMC layer tested at 100 MPa contact stress; 5—WC/Ti-6Al-4V coating prepared by single grain particles injection and tested at 100 MPa contact stress; e—experimental data, s—smoothed data.

Table 1 summarizes the test conditions and results from the wear measurements for SiC/Al-8Si. Specific wear rate k [10^{-6} mm³/Nm], which is the measure of removed volume per unit slide distance and unit load, was estimated by two different methods. Firstly, k_m was calculated from the mass loss of the pin, determined by weighing the pin before and after the test, taking into account the densities of the substrate alloys and the volume fraction of ceramic particles in the composites investigated [8,14,15]. Secondly, k_s was estimated from the slope of the wear curves in regions presenting a constant wear rate. Although k values determined by these two different methods are different for the same sample, they both clearly demonstrate the substantial increase in the wear resistance of the composite layer in comparison with the substrate alloy.

The same method was employed for all other MMC layers.

The wear and friction data for the WC/Ti-6Al-4V tests are also shown in Fig. 5. The tests for untreated and laser beam remelted Ti-6Al-4V substrates were aborted after 3 and 4 h, respectively, due to the very intensive wear. It is possible to conclude, that for both aluminium alloy and titanium alloy substrates (non-treated marked as 1 and laser beam remelted marked as 2), a transition period is present during which the wear rate is not constant and/or the friction coefficient is substantially changed as well. This behavior is not observed on the MMC samples, where neither the friction coefficient nor the wear rate experience substantial change during the wear process. The wear and friction results for the WC/Ti-6Al-4V coatings are summarized in

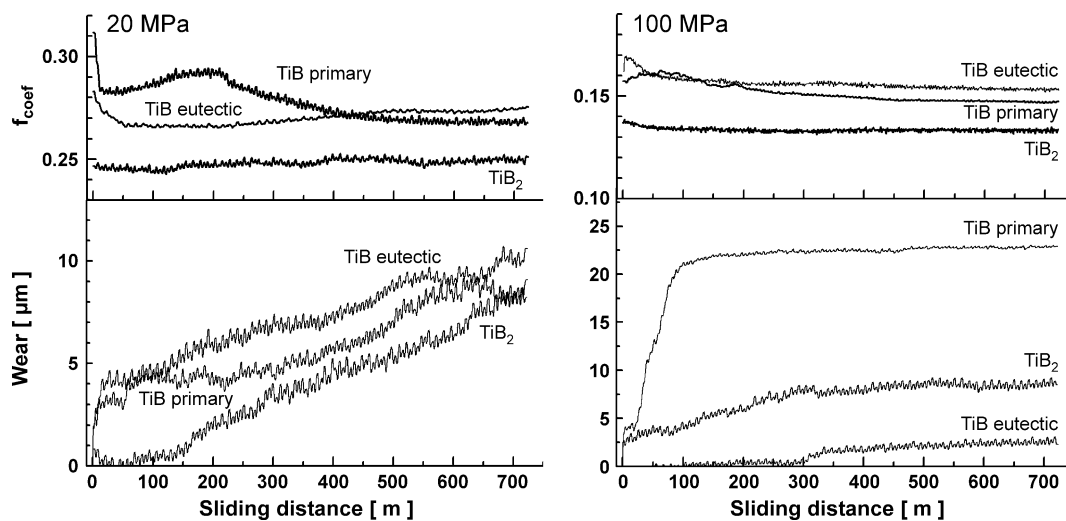


Fig. 6. Friction coefficient and wear versus sliding distance for TiB_x/Ti-6Al-4V MMC layers with different microstructures tested at 20 and 100 MPa contact stress.

Table 1

Test conditions, sliding wear and friction results for Al–Si substrate, laser beam remelted substrate and SiC/Al–8Si MMC

Sample	Contact stress [MPa]	k_m [10^{-6} mm ³ /Nm]	k_s [10^{-6} mm ³ /Nm]	f_a
Al–Si	20	13	6.0	0.14
Al–Si remelted	20	0.2	0.05	0.10
SiC/Al–Si	20	0.4	0.21	0.09
SiC/Al–Si	100	0.04	0.24	0.13

Table 2. The improvements in wear resistance are outstanding, and the friction coefficients of the MMC layers are significantly lower than those of the substrates.

Fig. 6 shows the sliding distance dependence, of friction coefficients and wear, for the TiB_x/Ti–6Al–4V MMCs, with different microstructures tested at 20 and 100 MPa contact stress. For the wear tests at 20 MPa, a correlation in the wear and friction results can be observed: coatings consisting of TiB₂ particles have the lowest wear depth, and the lowest friction coefficient. It comes as a surprise that for the TiB₂/Ti–6Al–4V coatings, a drastic increase of the wear rate occurs after a sliding distance of about 150m, whereby this increase of the wear rate is not seen in the friction coefficient, which remains more-or-less constant throughout the entire wear test.

Friction coefficients attained from the samples are most interesting when viewed in tandem with the wear data. The MMC consisting of primary TiB undergoes high initial wear, which is followed by increasing friction to around 200 m sliding distance. The friction coefficient then tails off corresponding to a more steady wear condition, until 550 m are reached and a slight jump occurs in the wear data, matched by a level of equilibrium apparent in the frictional coefficient.

The sample with a eutectic microstructure presents an initial decrease of the friction coefficient combined by a sharp wear increase. After a sliding distance of about 50m, only a very small value of the friction coefficient and only minor changes in the wear rate are observed. It appears that the friction coefficient reaches a plateau at a sliding distance of about 550 m.

Table 2

Test conditions, sliding wear and friction results for Ti–Al–V substrate, laser beam remelted substrate and WC/Ti–6Al–4V MMCs

Sample	Contact stress [MPa]	k_m [10^{-6} mm ³ /Nm]	k_s [10^{-6} mm ³ /Nm]	f_a
Ti–Al–V	20	189	269	0.21
Ti–Al–V remelted	20	40	240	0.18
WC/Ti–Al–V layer	20	0.13	0.50	0.11
WC/Ti–Al–V layer	100	0.08	0.05	0.12
WC/Ti–Al–V ^a layer	100	<0.01	0.038	0.12

^a Denotes the layer prepared by injection of single grained WC particles with a microstructure depicted in **Fig. 3**.

The results attained for the 100 MPa contact pressure condition come as a surprise, since the same correlations as previously observed do not occur. This said, there is the obvious correlation for TiB eutectic sample, whose friction coefficient is the highest, but whose wear is the lowest. Conversely TiB₂ sample exhibits the lowest coefficient of friction, yet the wear is still acceptable, whilst sample with TiB primary microstructure portrays incredible wear in the early stages, which then becomes stable. This must be attributed to a sharp increase in temperature, which readily induces oxide formation, thus instigating oxidative wear, and consequently low wear rates. This would appear to hold benefits for service where long endurance is paramount, but may cause severe problems in cyclic loading conditions.

A summary of the wear and friction coefficient results for the TiB_x/Ti–6Al–4V MMCs is presented in **Table 3**, and again highlights that excellent wear resistance results can be achieved with laser processing. The poor frictional properties delivered by the coatings at low loads are very surprising, but an attempt to explain the phenomenon will be made in due course.

3.3. Worn morphologies

SEM and EDS observations were employed to examine the morphology and the composition of the worn surfaces of all samples. As expected, the hard aluminum oxide layer formed during laser remelting causes a pronounced wear improvement of the laser remelted Al–8Si surface, although the thickness of this layer is limited [8].

The worn surface of SiC/Al–8Si and WC/Ti–6Al–4V layers tested at 20 MPa contact stress show an eroded wear surface morphology between the strengthening particles, with a few of them protruding from the surface. **Fig. 7** demonstrates an oblique view on a couple of such particles on the SiC/Al–8Si worn surface. The black arrows indicate the protruding areas of the ceramic particles, which were in a direct contact with the disk just before the wear test was stopped. The BSE image shown in **Fig. 7b** highlights the presence of iron-based debris collected on the worn surface as a micro-cutting product near the edges of the SiC

Table 3

Test conditions, sliding wear and friction results for TiB_x/Ti–6Al–4V coatings

Sample	Contact stress [MPa]	k_m [10^{-6} mm ³ /Nm]	k_s [10^{-6} mm ³ /Nm]	k_{st} [10^{-6} mm ³ /Nm]	f_a
Ti–Al–V	20	189	269	–	0.21
TiB ₂ /Ti–Al–V	20	0.16	0.61	0.3	0.25
Eutectic TiB/Ti–Al–V	20	0.13	0.74	0.35	0.27
Primary TiB/Ti–Al–V	20	0.44	0.7	0.52	0.28
TiB ₂ /Ti–Al–V	100	0.069	0.02	0.023	0.13
Eutectic TiB/Ti–Al–V	100	0.13	0.03	0.03	0.16
Primary TiB/Ti–Al–V	100	0.48	0.02	0.02	0.15

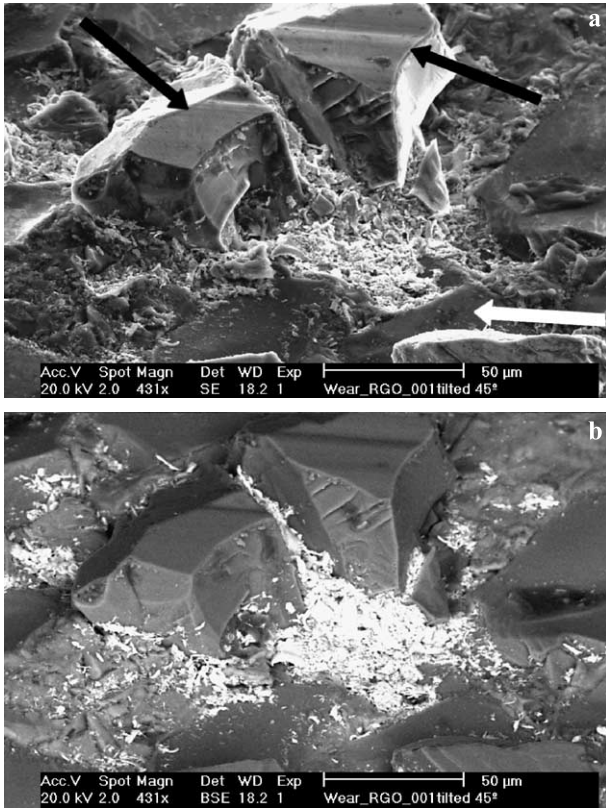


Fig. 7. Oblique SEM view in SE (a) and BSE (b) mode on the same place of worn surface of SiC/Al–8Si layer. The white arrow indicates the wear direction; the black arrows show the top surfaces of strengthening particle, which were in a contact with disk just before the end of wear test.

particles. The wear of the SiC particles proceeds by a combination of two mechanisms: the slow abrasive wear on the contact surface combined with the fast cleavage of the exposed SiC particles. Cleaved surfaces are visible on the sides of these particles, as well as on the particles, which were not in a direct contact with the disk just before the wear test was stopped, because they were partially cleaved out previously. Small steps observable on the wear curves also support the presence of such a mechanism.

Previous analysis [9] of worn surfaces of WC/Ti–6Al–4V layers tested at 20 MPa and 100 MPa contact stress drew conclusions with respect to their morphology and qualitative composition. The wear surface of the layer tested at 100 MPa contact stress shows a relatively flat morphology near the front edge of the wear surface. In the second part of the wear surface the rougher area is present with deeply eroded regions between embedded WC particles. BSE investigation [9] clearly demonstrated that fragments of heavy particles (WC) continuously cover the flat part of the wear surface and that inside the rough zone individual WC particles were upraised from the eroded Ti alloy substrate. The number of particles present on the wear surface was still quite high. On the other hand, the wear surface of the layer tested at 20 MPa contact stress showed only an “eroded” wear surface morphology, with just a few WC protrusions being in

contact with the steel disc. The total size of such areas forms only a small fraction of the whole wear surface and therefore the actual contact stress was much higher than the value of 20 MPa calculated from the applied normal force and sample dimensions. This once again highlights the complexity of wear processes and the consequent limitations in the evaluation of wear. It was concluded [9] that wear of WC particles proceeds by inter-granular brittle fracture and that “the most wear resistant” area is a hard surrounding of WC particle formed by TiC dendrites, shown in Fig. 2b.

A completely different picture can be observed on the worn surface of WC/Ti–6Al–4V coating prepared by injection of single grained WC particles and tested at contact stress of 100 MPa (see Fig. 8b). The density of WC particles on the worn surface corresponds to the density observed in microstructural observations, which means that all embedded WC particles join together in the wear process and stay on the wear surface without any loss. The insert in Fig. 8b clearly demonstrates that the main wear mechanism is now controlled by a localized damage of WC particles through an accumulation of plastic deformation in a system of slip bands. The orientation of these slip systems towards the wear direction differs from one single particle to another and therefore the damage “features” on particle surfaces are

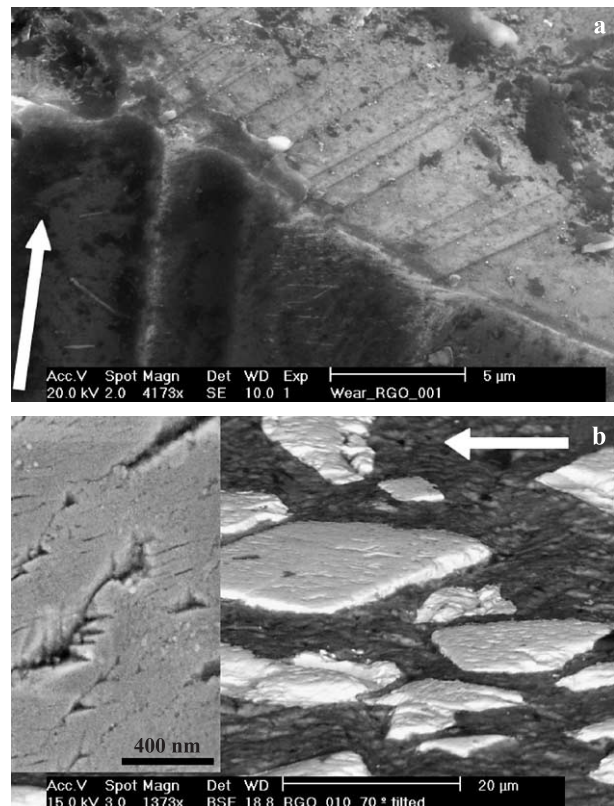


Fig. 8. SEM micrographs of worn surfaces of (a) SiC/Al–8Si and single grained (b) WC/Ti–6Al–4V MMC layers tested at contact stress of 100 MPa. The white arrows indicate the wear direction. Insert in (b) is the high resolution SEM micrograph from the worn surface of single grain WC particle.

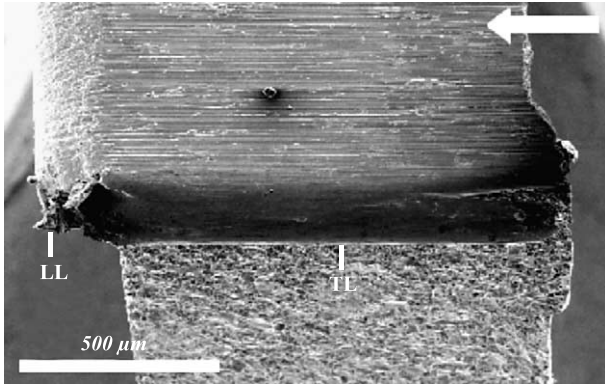


Fig. 9. Lip formation of untreated Ti-6Al-4V after a sliding wear test at 20 MPa contact pressure. Arrow indicates wear direction; LL—longitudinal lip, TL—transverse lip.

also different. The insert in Fig. 8b shows the small triangles formed at the intersection of two slip systems as an initial damage place. The traces of localized plastic deformation are also visible near the edge of a SiC particle on the SiC/Al-8Si worn surface (Fig. 8a). The white arrow indicates the wear direction on the contact surface with worn grooves. A parallel system of shear bands is visible on the free surface of the particles.

The non-treated Ti-6Al-4V surface was tested only at 20 MPa and the worn surface is shown in Figs. 9 and 10. A

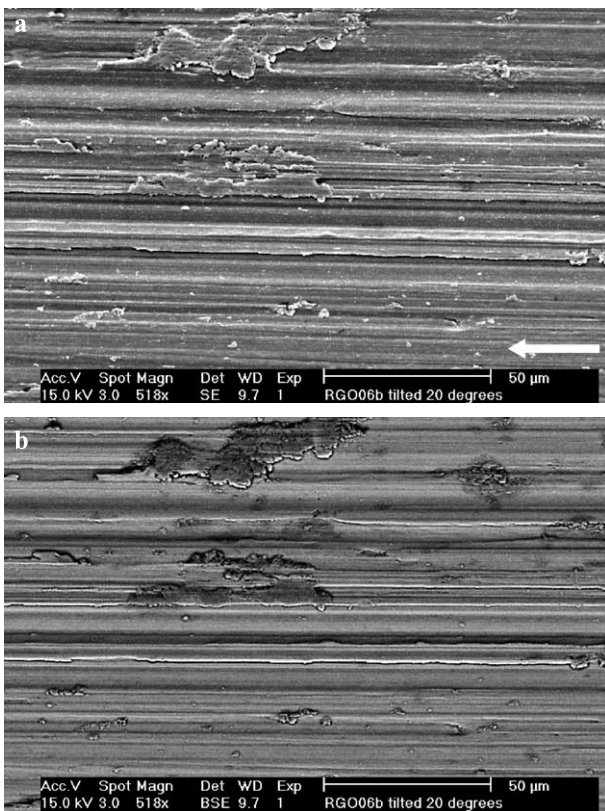


Fig. 10. SEM micrographs exhibiting (a) directional ductile wear of Ti-6Al-4V alloy and oxide island formations, shown as darker regions under (b) BSE investigation. Arrow indicates wear direction.

very interesting lip formation is apparent at the exit edge of the sample, which clearly indicates ductile smearing of the Ti-6Al-4V due to thermal effects. The lip is apparent along three sides of the sample, see Fig. 9. However, the appearance in the longitudinal direction (LL) is very different from that in the transverse (TL). Other areas, as those in Fig. 10, represent delamination of the substrate, represented by the oxidized islands seen slightly darker under BSE mode inspection (Fig. 10b). This phenomenon is in clear accordance with other previous studies on sliding wear of untreated Ti-6Al-4V substrates [18–20].

Surface deformation by ductile layering is noticeable, on the untreated (Fig. 10), primary TiB (Fig. 11) and eutectic TiB samples, which is, in part the result of smearing, and also the formation of peaks, which are subsequently flattened. Fig. 11b, highlights the high density of plastic deformation accumulated at the edges of the flattened layers, which may result in material removal by chipping.

As a means of qualifying the SEM work, confocal microscopy was implemented and the results are presented in Fig. 12. It is clear that some areas display incredible smoothness, whilst the area where a peak and a trough are formed shows quite large surface amplitudes (on average this was found to be 5 μm). It is proposed that the wear behavior of this sample involves a constant formation and flattening of these peak and trough couplings.

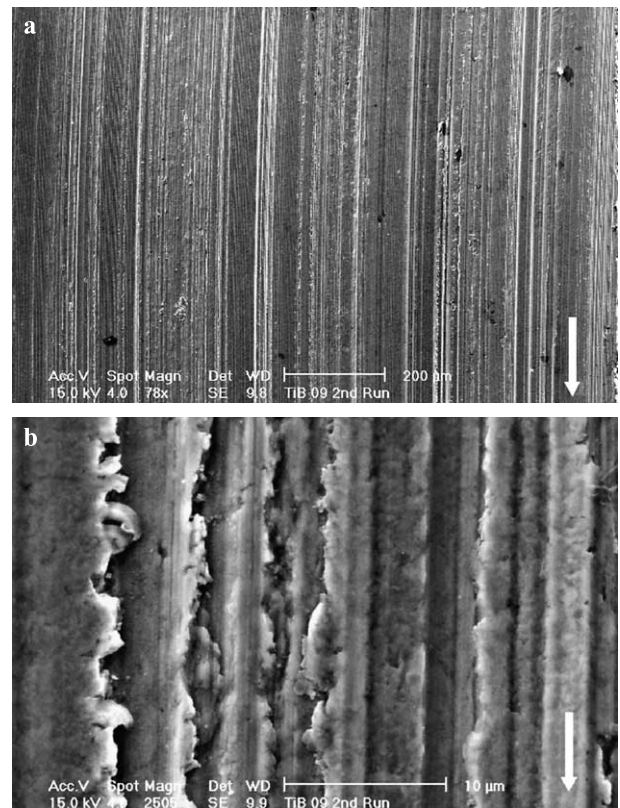


Fig. 11. SEM micrographs of the worn surface of primary TiB layer after 100 MPa sliding wear test. Arrows indicate wear direction.

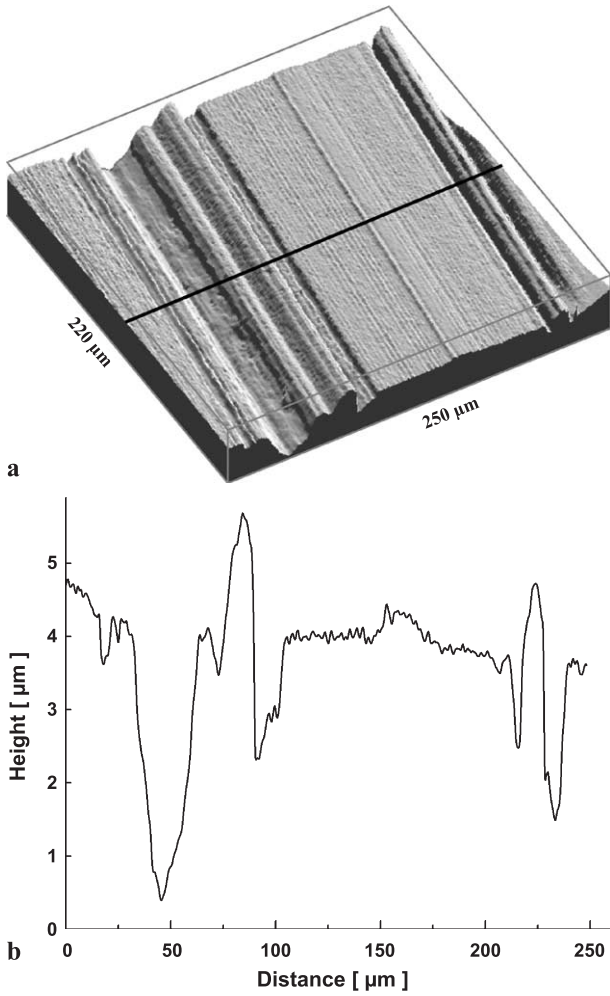


Fig. 12. Confocal microscopy of worn surface for primary TiB sample; (a) photorealistic image of worn surface; (b) height profile in direction perpendicular to wear direction along the marked line.

The SEM micrograph of a worn surface for the sample with eutectic TiB microstructure is shown in Fig. 13. This SEM micrograph is representative of the overall features and shows how an individual TiB₂ particle, which does not

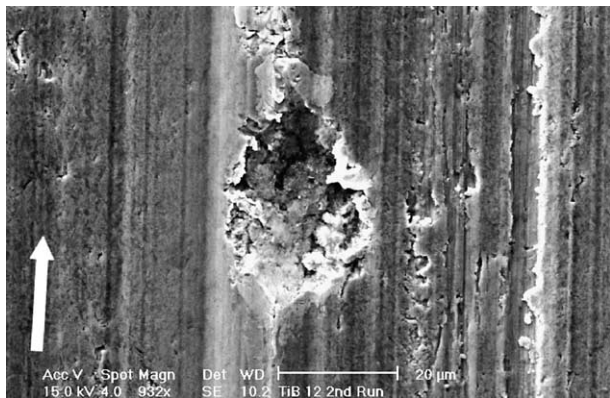


Fig. 13. SEM micrograph of the worn surface of eutectic TiB layer after 100 MPa sliding wear test. Arrow indicates wear direction.

undergo full solid solution, can cause problems to the final worn surface. Some of the original eutectic features were still visible in BSE mode. The EDS elemental mappings expose the flaw of a particle, which was removed. Subsequently, the void left was filled with material removed from the steel disc. Confocal microscopy was again utilized to complement the SEM and although the appearance of the surface is rougher than that of the primary TiB sample, the range is much more shallow, only 2.5 μm, and this is important since the actual material removed (from Fig. 6 for 100 MPa) is only of this order, implying that wear becomes more or less negligible.

A very different microstructure of the worn surface is seen in Fig. 14, but once again, uniform grooving is dominant. Fig. 14b highlights the details around the TiB₂ particle, showing again how the particles undergo brittle fracture, since they are well bound to the matrix. This image also represents the way in which the peaks are flattened since there is clearly visible one longitudinal region where the flattened material direction is at angle to the wear direction. The elliptical white inserts in Fig. 14b show the iron rich regions of the worn surface. Oxides were detected on the whole surface shown in Fig. 14b, apart from regions where the dark boride particles are present. This

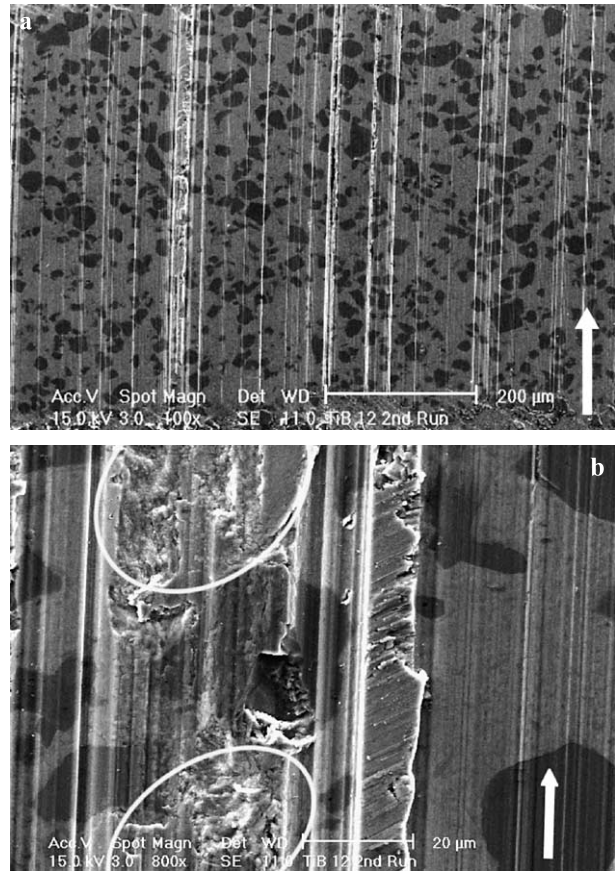


Fig. 14. SEM micrograph of worn surface of TiB₂/Ti-6Al-4V (a) overview with TiB₂ particles distribution; (b) detail region selected for elemental mapping with two elliptical Fe rich areas highlighted. Arrows indicate wear direction.

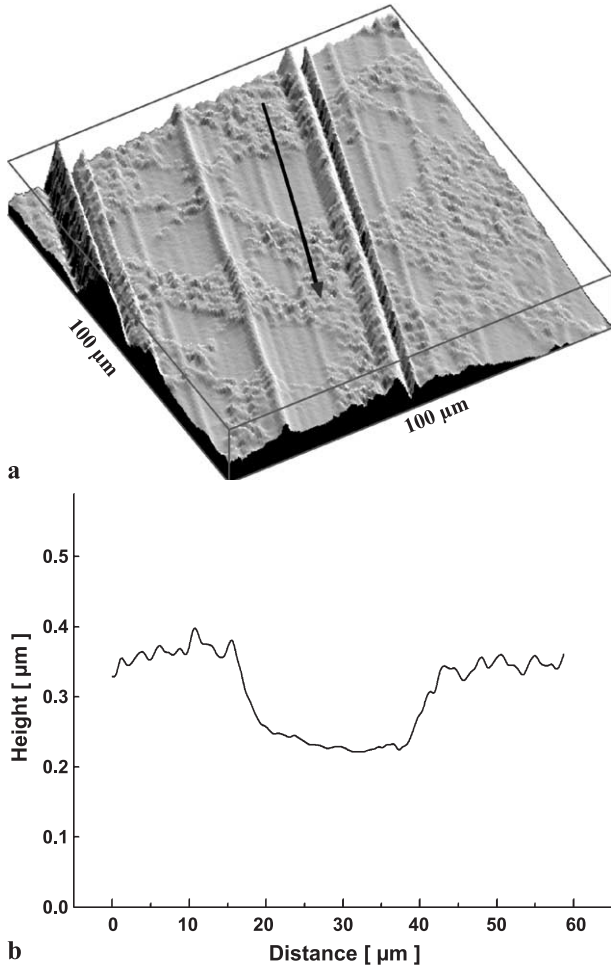


Fig. 15. Confocal microscopy of worn surface for TiB_2 sample; (a) photorealistic image of worn surface; (b) height profile in wear direction along the marked line.

oxygen build-up became clearly highlighted when the complementary confocal microscopy (Fig. 15) was undertaken. They are the regions located higher than the hard TiB_2 particles.

4. Discussion

Past and current literature state that under boundary lubrication conditions, MMC materials could easily compete with qualified tribomaterials [21,22]. As Hutchings et al. [23] reported, numerous investigations of the sliding wear of aluminum matrix composites against steel have shown significant increases in their wear resistance compared with unreinforced aluminum alloys. SiC/Al–8Si MMC coating tested at low contact load shows that SiC reinforcing particles tend to support the contact stresses. The worn surfaces exhibited SiC particles protruding from the matrix alloy (see Fig. 7). During sliding the exposed portions of these particles created a local abrasive action on the steel countersurface. As a consequence, steel frag-

ments were transferred to the composite surface (Fig. 7b) and sometimes they form a protective, iron rich transfer layer. However, exposed SiC particles can become cleaved (Fig. 7a) and these cleaved parts act as third body abrasives, which accelerate the wear. Thus the mechanisms (a) and (b) denoted in Fig. 16 were observed for the SiC/Al–8Si MMC formed by laser melt injection.

Another type of brittle fracture of embedded particles was detected during wear of the multi grain WC/Ti–6Al–4V MMC [9]. The inspection of wear surfaces of WC/Ti–6Al–4V alloy layer by SEM brought to light that hard phase TiC

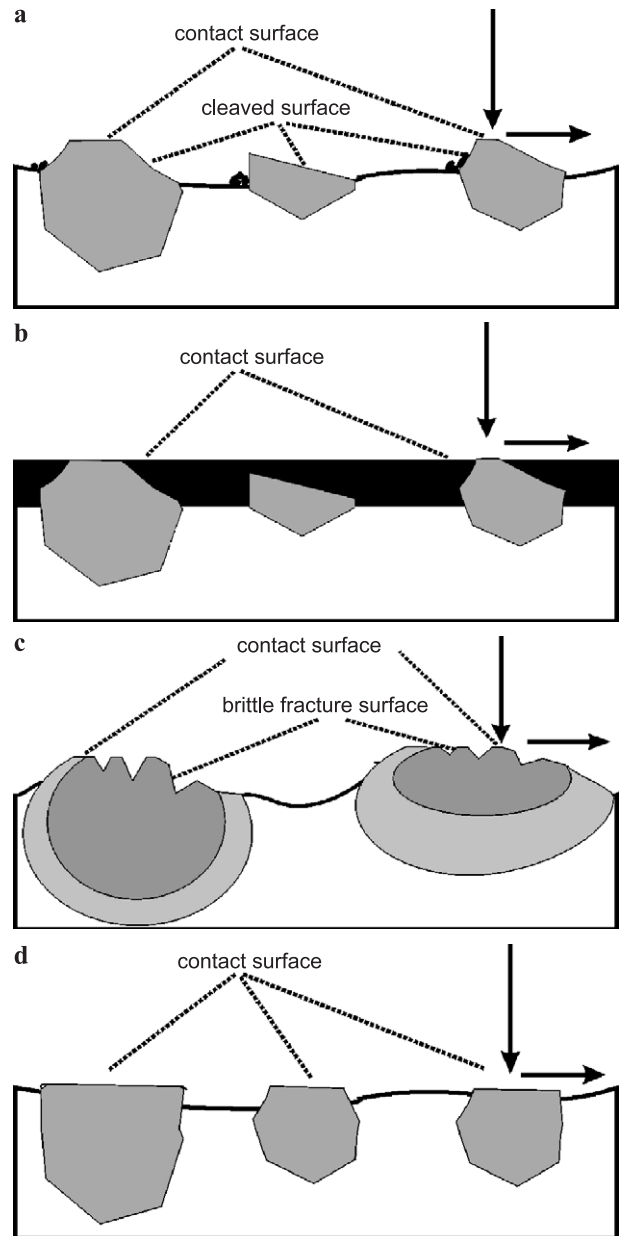


Fig. 16. Schematics of main wear mechanisms observed on worn surfaces of MMC prepared by laser surface engineering techniques. Main mechanisms characteristic for: (a) SiC/Al–8Si MMC; (b) SiC/Al–8Si, $TiB_2/Ti-6Al-4V$ and $TiB/Ti-6Al-4V$ MMCs; (c) fused multigrain WC/Ti–6Al–4V MMC; (d) single grain WC/Ti–6Al–4V MMC.

formed on the particle/substrate interface and also inside the substrate itself is responsible for substantial sliding wear improvement. On the contrary, when an embedded fused WC particle is exposed on the wear surface, it starts to crumble through the intergranular brittle fracture of individual grains inside one WC particle. It was concluded [9] that fused WC particles become to be the weakest link in WC/Ti–6Al–4V layer microstructure, similarly as in the case of the tensile properties of this material [15], where the crack nucleation process is controlled mainly by intergranular brittle fracture within WC particles. In this case, mechanisms (b) and (c) from Fig. 16 control the wear.

Completely different mechanical characteristics can be expected for the same MMC layer prepared by injection of single grain WC particles. Owing to a good incorporation of WC particles into matrix (proved by an existence of crystallographic orientation relationships between embedded particles and surrounding phases) and very good wear characteristics of WC, a further improvement in wear resistance can be expected. As the insert in Fig. 8b shows, the size of hard debris must be much smaller than reinforced WC particles itself, therefore the abrasive wear does not expose particles from the matrix and the main wear mechanism is a localized plastic damage on WC particles, schematically shown in Fig. 16d.

The microstructures of TiB_x/Ti–6Al–4V layers prepared by laser cladding and laser melt injection have been shown to exhibit excellent interfacial bonding between the primary TiB, eutectic and TiB₂ particles [14,24]. This provides initial explanation for the uniform wear behavior prevalent in all samples, with the microstructural particle distribution seemingly being more important than the amount of hard-particle addition. The eutectic sample, however, is not wholly homogeneous, as few TiB₂ particles, unaffected by the laser treatment, are seen to become embedded in the microstructure, with very poor bonding. These particles are easily removed from the matrix since the homogeneous eutectic microstructure is formed upon rapid solidification. Dendritic growth is seen to stop short around these larger particles (Fig. 13), and once they are removed, they become third bodies in the wear mode, leading to deep grooving and essentially avoidable material removal. If a TiB₂ particle is well bound to the Ti–6Al–4V matrix, as witnessed in Fig. 14b, then the particle is not removed due to particle pull-out, but instead brittle fracture of the particle is witnessed.

A reaction zone is notably surrounding the TiB₂ particle (Fig. 4a), which consists of TiB, due to boron diffusion from the TiB₂ particle into the matrix, providing an excellent bonding, in a similar fashion as that witnessed for the WC/Ti–6Al–4V MMC [9]. On the whole, the load bearing capability of the material, induced through the hard TiB₂ particles, assures even wear, as these support the load and are seen to be polished in appearance, since the mating material asperities are not large enough to significantly weaken/remove the soft matrix and consequently cause these large hard particles to be plucked from the material.

Instead, the matrix material merely appears roughened and stands proud of the TiB₂ particles by approximately 0.1 μm (Fig. 15b). This must be due to oxidation effects since the elemental mapping shows oxidative coverage in all regions except the TiB₂ particles.

Both the eutectic and primary TiB coatings exhibit surface oxidation, leading to oxidative wear. It is induced through thermal oxidation of the surface ‘hotspots’ or asperity contact areas and oxidative wear becomes the contact condition, which suppresses the plastically dominated wear mechanisms and induces delamination due to the reduced shear strength of the metal–oxide interface. This may be considered as a reason for the reduction in friction for the higher loads, and also for the reduced wear response, in particular that of the eutectic TiB sample.

Several schematic models have been developed and discussed thus far, and it is suggested that model (b) from Fig. 16 is most appropriate to all three TiB_x/Ti–6Al–4V coatings, with the dark region being representative of an area affected by the wear. Obviously the eutectic needles in the regime are much smaller than the large particles in the model, and do not support the load in the manner of the TiB₂/Ti–6Al–4V sample in the same way, but the fundamental principle holds true.

Generally, if loads are light and the natural spontaneous oxidation of a metal can keep up with the rate of its removal by wear, then that wear rate will be relatively low (the oxide acting as a lubricant), then mild wear is said to be in effect. If loads are high and the protective oxide is unable to form effectively, thus permitting intimate metallic contact and adhesion, then the wear rate will be high, namely severe wear; however, as described in Ref. [25], increased loads can easily reform to a mild regime. 100 MPa pressures could cause this transition, and 20 MPa may easily fit within the severe regime, which may explain the reduced wear rates attained at higher loads.

Thin, brittle oxide forming materials, notably stainless steel, aluminum alloys and titanium, produce protective oxides that can be disrupted and the consequent massive adhesion and wear is called galling, as seen in the untreated (Fig. 10) and remelted samples.

Mild wear is characteristic of dry sliding metals where the conditions are such that the naturally protecting oxide can continuously reform at the sliding contact, so acting with a degree of dry lubrication and reducing the wear rate. It also occurs with hardened alloys (usually steels) when, even under high contact loads and high speeds, the underlying substrate can support the oxide and prevent its disruption by deformation below it [25].

Severe wear occurs (generally in soft metals or alloys) when the conditions are such that the oxide is disrupted at a greater rate than which it can reform, so that clean metal is exposed below and massive adhesion occurs between the mating surfaces. It is common for soft materials to show sudden transitions between these two wear regimes. At high loads, the frictional heating is such that the oxidation rate

rapidly increases and can again form a protective layer; and mild wear is re-established. This accounts for the improvement in the treated samples, since the substrate is able to support the oxide layers formed through the addition of the hard ($\text{TiB}_2=35$ GPa at 20 °C, 7.5 GPa at 800 °C) [26] particles and the uniform distributions.

To provide an explanation of the substantial differences in specific wear rates k_m and k_s calculated by two distinct methods in Tables 1, 2 and 3, the analysis of their origins of error is of primary importance. Pin mass loss calculation is an integral method, which includes an initial stage of the wear process when the wear rate can change substantially. Therefore, this will lead to a k_m value higher than k_s for the eutectic Al–Si substrate (curve 1e in Fig. 5) and primary TiB (100 MPa in Fig. 6) because during the run-in process the wear rate decreases. On the other hand, for Ti–6Al–4V and Ti–6Al–4V remelted substrates (curves 1e and 2e in Fig. 5), the wear rate in an initial period is smaller than the final wear rate, therefore k_m is seen to be smaller than k_s for these substrates. A small difference in initial wear behavior of non-treated and laser remelted Ti–6Al–4V alloy can be explained by the formation of a thin (~30 μm) and more wear resistant layer during laser remelting on the top of laser melt pool due to non-ideal gas shielding. Formation of such wear resistant coatings reinforced by hard TiN dendrites after remelting Ti alloy in nitrogen atmosphere was already reported [18,27].

Another inaccuracy of calculating wear rate from the mass loss is connected with possible mass transfer from steel disk to sample pin. This is witnessed very often in MMC layers, when hard particles, which protrude from the metal surface, perform an abrasive micro-machining with joint mass transfer. Sometimes this mass transfer is so extensive that it forms a protective layer in inter-particulate regions, as model (b) in Fig. 16 demonstrates. The mass loss method also supposes a constant particles density in metal matrix and non-selective wear between matrix and particles, which is incorrect.

The values attained using the k_s method can be corrected for true contact areas, which lead to true contact stresses, and these values are termed k_{st} . The inspection after wear test show, for instance, that the surface of the $\text{TiB}_2/\text{Ti–6Al–4V}$ sample subsequent to the 20MPa test was only around 50% of the supposed contact area, which leads to huge deficiencies in the k_m calculation which cannot be remedied since the actual contact stress becomes twice the nominal contact stress.

Therefore, it seems that the slope method provides a more accurate estimation of wear rate, although k_s also includes wear of the disk. The amount of wear of disks was controlled by the mass loss method and it was confirmed that wear of discs is always under the detectable limit, i.e. $k_{\text{disk}} < 0.01 \times 10^{-6} \text{ mm}^3/\text{Nm}$. However, k_s value is overcast with a quite large error, especially for samples with high wear resistance, as is seen for eutectic sample under high loads, where once initial wear is removed from consid-

Table 4

Relative wear resistance of different MMC layers produced by laser surface engineering technique

Sample	RWR		
	k_m	k_s	k_{st}
Al–Si remelted	65	120	–
SiC/Al–Si	32.5	28.6	–
Ti–Al–V remelted	4.7	1.1	–
WC/Ti–Al–V layer	1454	538	–
WC/Ti–Al–V layer ^a	>18,900 ^a	7000 ^a	–
$\text{TiB}_2/\text{Ti–Al–V}$	1181	441	897
eutectic TiB/Ti–Al–V	1454	364	769
primary TiB/Ti–Al–V	429	384	517

^a Denotes MMC with single grain WC particles. RWR for this MMC obtained by comparison with substrate tested at 20 MPa, while MMC was tested at 100 MPa.

eration; all three samples portray comparable wear resistance. This is clearly not so if the shape of the curves and area under the curves are considered and is notably highlighted when one likes to quantify wear resistance improvements. Such benefits in reduced wear rate in MMC can be usefully described by a “Relative Wear Resistance” (RWR) defined as the wear rate of the unreinforced matrix divided by that of the MMC under the same wear conditions [23]. RWR improvement reaches values of 29–33 for SiC/Al–Si MMC, 500–1500 for multigrain WC/Ti–6Al–4V MMC and 400–1500 for $\text{TiB}_x/\text{Ti–6Al–4V}$ MMCs, as seen in Table 4.

5. Conclusions

Laser cladding and laser melt injection are very suitable techniques for producing metal matrix composite coatings on Al–8Si and Ti–6Al–4V alloys. The amount of ceramic particles is sufficient to reinforce the matrix and the particles are distributed over the whole depth and width of the melt pool. During the laser melt injection, new phases are formed mainly on particle/matrix interfaces, often with orientation relationships to the injected particles, which provide a good bonding between particles and the matrix.

A substantial improvement in sliding wear resistance under boundary lubrication conditions is observed for SiC/Al–8Si; WC/Ti–6Al–4V and $\text{TiB}_2/\text{Ti–6Al–4V}$ surface layers prepared by the laser melt injection technique in comparison with substrate alloys. The sliding wear of SiC/Al–8Si MMC proceeds mainly through the cleavage of SiC particles, which are in direct contact with the disc and which are not supported by the wear debris or the matrix. The highest wear improvement of WC/Ti–6Al–4V MMC was detected for MMC layer prepared by injection of single grain WC particles, which do not produce large third body debris as in the case of fused WC particles or cleaved SiC particles. Wear in this case proceeds through a very localized plastic deformation on the contact surface of WC particles. Surface oxidation of the Ti–6Al–4V matrix coupled with the load

support provided by TiB₂ particles lead to the most protective wear mechanism.

Outstanding sliding wear resistance and friction improvements have also been obtained by the fabrication of TiB/Ti–6Al–4V by a laser cladding process. The layers are again found to be extremely adherent and large areas can be covered with the application of multiple adjacent tracks. One of the reasons for this superb adherence is attributed to the excellent interfacial bonding between the in-situ formed TiB and the Ti–6Al–4V matrix.

The best combination of TiB₂/TiB particles and Ti–6Al–4V for good wear resistance is seen to depend upon the loading conditions, with TiB₂/Ti–6Al–4V performing best at low loads (20 MPa), while the eutectic microstructure of TiB/Ti–6Al–4V demonstrates good resistance under the 100 MPa loading condition.

Acknowledgements

Financial support from the foundation for Fundamental Research on Matter (FOM-Utrecht) and the Netherlands Institute for Metals Research are gratefully acknowledged. The authors are grateful to TNO Eindhoven who kindly performed the wear tests and to Damiano Galvan for stimulating discussion.

References

- [1] A. Bloyce, P.H. Morton, T. Bell, *Surface Engineering of Titanium and Titanium Alloys*, ASM Handbook, vol. 5, 1996, p. 835.
- [2] J.H. Abboud, D.R.F. West, *J. Mater. Sci. Lett.* 10 (1991) 1149.
- [3] J.A. Vreeling, *Laser Melt Injection of Ceramic Particles in Metals* (PhD thesis), Groningen, Groningen University Press 2001, 136 pp.
- [4] F. Delannay, L. Froyen, A. Deruyttere, *J. Mater. Sci.* 22 (1987) 1.
- [5] X.B. Zhou, J.Th.M. De Hosson, *Acta Mater.* 44 (1996) 421.
- [6] B.J. Kooi, M. Kabel, A.B. Kloosterman, J.Th.M. De Hosson, *Acta Mater.* 47 (1999) 3105.
- [7] K.P. Cooper, P.L. Slebodnick, K.E. Lucas, E.A. Hogan, *J. Mater. Sci.* 33 (1998) 3805.
- [8] J.A. Vreeling, V. Ocelik, Y.T. Pei, D.T.L. Van Agterveld, J.Th.M. De Hosson, *Acta Mater.* 48 (2000) 4225.
- [9] J.A. Vreeling, V. Ocelik, J.Th.M. De Hosson, *Acta Mater.* 50 (2002) 4913.
- [10] Y.T. Pei, V. Ocelik, J.Th.M. De Hosson, *Acta Mater.* 50 (2002) 2035.
- [11] J.Th.M. De Hosson, B. Kooi, in: H.S. Nalwa (Ed.), *Handbook of Surfaces and Interfaces in Materials*, vol. 1, Academic Press, 2001, p. 1, chap. 1.
- [12] R. Banerjee, P.C. Collins, A. Genc, H.L. Fraser, *Mater. Sci. Eng., A* A358 (2003) 343.
- [13] V. Ocelik, J.A. Vreeling, J.Th.M. De Hosson, *J. Mater. Sci.* 36 (2001) 4845.
- [14] D. Galvan, V. Ocelik, Y. Pei, B.J. Kooi, J.Th.M. De Hosson, *Proceedings of the 22nd Heat Treating Society Conference and the 2nd International Surface Engineering Congress*, 15–17 September 2003, Indianapolis, Indiana, USA, ASM International, 2004, p. 412.
- [15] V. Ocelik, J.A. Vreeling, J.Th.M. De Hosson, in: C.A. Brebbia (Ed.), *Surface Treatment V: Computer Methods and Experimental Measurements for Surface Treatment Effects*, WIT Press, Southampton, 2001, p. 151.
- [16] J.Th.M. De Hosson, V. Ocelik, *Mat. Sci. Forum* 426–432 (2003) 123.
- [17] A. Savitzky, M.J.E. Golay, *Anal. Chem.* 36 (1964) 1627.
- [18] K.G. Budinski, *Wear* 151 (1991) 203.
- [19] A. Molinari, G. Staffelini, B. Tesi, T. Bacci, *Wear* 208 (1997) 105.
- [20] P. Jiang, X.L. He, X.X. Li, L.G. Yu, H.M. Wang, *Surf. Coat. Technol.* 130 (2000) 24.
- [21] S.C. Tjong, Z.Y. Ma, *Mater. Sci. Eng.* 29 (2000) 49.
- [22] A. Yakovlev, Ph. Bertrand, I. Smurov, in: T.S. Sudarshan, S.V. Joshi, G. Totten (Eds.), *Surface Treatment: Research and Applications*, ARCI Hyderabad, India, 2003, in press.
- [23] I.M. Hutchings, S. Wilson, A.T. Alpas, in: A. Kelly, C. Zweben (Eds.), *Comprehensive Composite Materials*, Pergamon, Amsterdam, 2000, p. 3.19.
- [24] A. Agarwal, N.B. Dahotre, *Adv. Mater. Process.* 157 (2000) 43.
- [25] R.D. Arnell, P.B. Davies, J. Halling, T.L. Whomes, *Tribology. Principles and Design Applications*, Macmillan, London, 1991, 255 pp.
- [26] NIST ceramic database: www.ceramics.nist.gov/srd/summary/scdtib2.htm.
- [27] A.B. Kloosterman, J.Th.M. De Hosson, *Scr. Metall. Mater.* 33 (1995) 567.